Supporting Information

Constructing layered double hydroxides derived heterogeneous $Ti_3C_2T_x$@S-MCoP (M=Ni, Mn, Zn) with S-vacancies to boost sodium storage performance

Qun Li [a], Qingze jiao [a,c], Huanjun Li [a], Yu Yan [b], Chengxing Lu [b], Xueran Shen [a], Tingting Gu [a], Wei Zhou [b,*], Yun Zhao [a], Hansheng Li [a], and Caihong Feng [a,*]

[a]School of Chemistry and Chemical Engineering, Beijing Key Laboratory for Chemical Power Source and Green Catalysis, Beijing Institute of Technology, Beijing 10081, China

[b]School of Chemistry, Beijing Advanced Innovation Center for Biomedical Engineering, Beihang University, Beijing 100191, China

[c]School of Materials and Environment, Beijing Institute of Technology (Zhuhai Campus), Zhuhai 519085, China

*Corresponding author E-mail: zhouwei@buaa.edu.cn (Wei Zhou), fengch@bit.edu.cn (Caihong Feng)

Supporting Figures and Tables

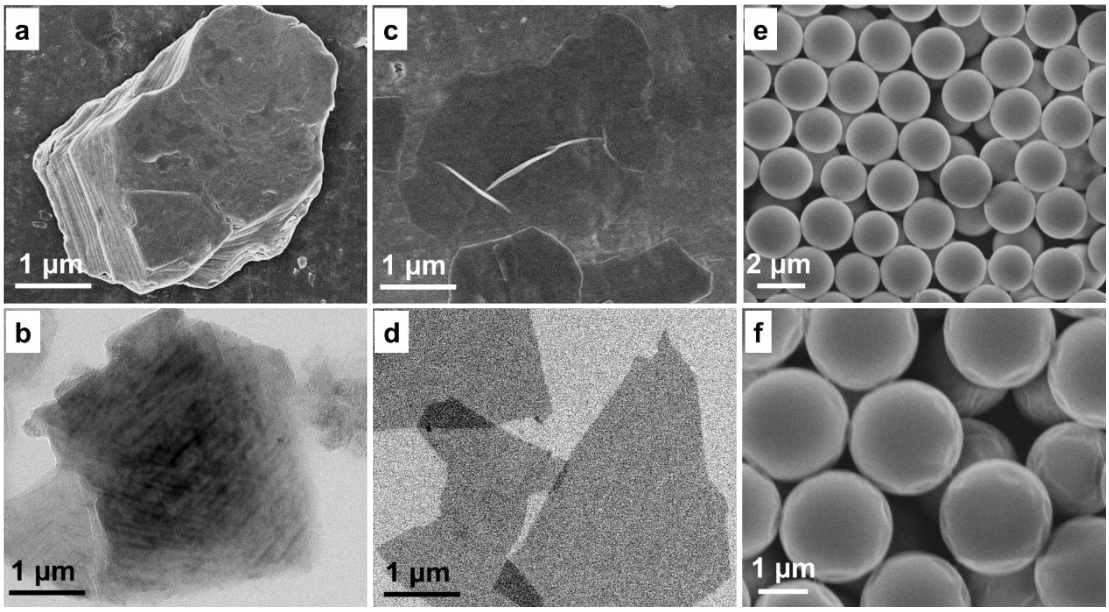

Fig. S1. (a)-(b) SEM and TEM images of MAX. (c)-(d) SEM and TEM images of $Ti_3C_2T_x$ MXene. (e)-(f) SEM images of PMMA spheres.

As shown in **Fig. S1a-b**, the Ti_3AlC_2 MAX exhibits a typical massive morphology with a smooth surface. After LiF and HCl etching and ultrasonic exfoliation, the bulk structure is transformed into a typical two-dimensional nanosheets, indicating the $Ti_3C_2T_x$ is successfully prepared (**Fig. S1c-d**). The as-prepared PMMA spheres possess an average size of 2 μm with smooth surface (**Fig. S1e-f**).

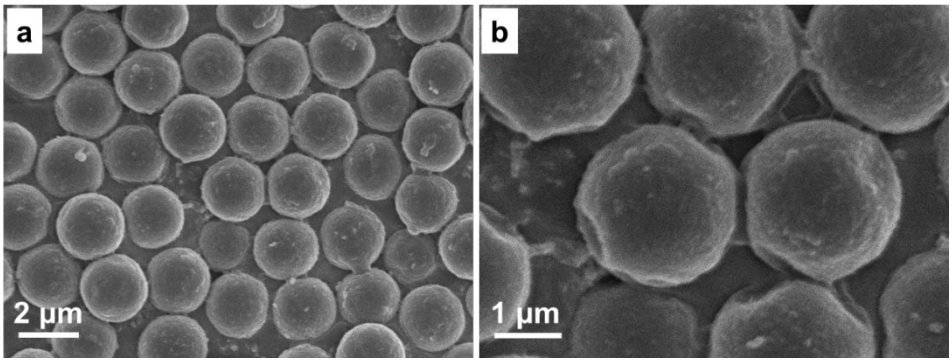

Fig. S2. SEM images of PMMA@$Ti_3C_2T_x$.

As shown in **Fig. S2**, after $Ti_3C_2T_x$ wrapping, the surface of PMMA@$Ti_3C_2T_x$ spheres becomes rough with an average size of 2 μm.

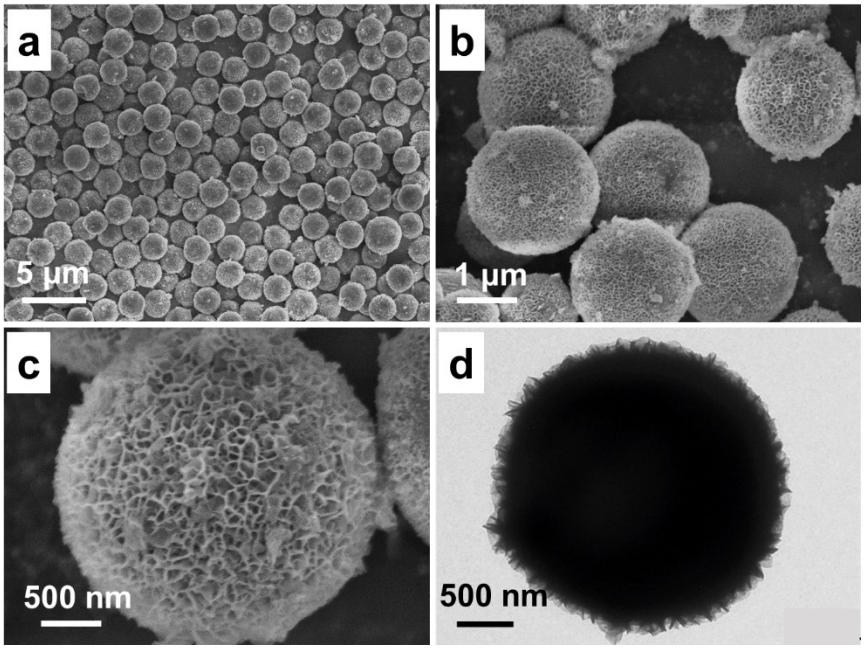

Fig. S3. (a)-(c) SEM images of PMMA@$Ti_3C_2T_x$@NiCo-LDHs. (d) TEM image of PMMA@$Ti_3C_2T_x$@NiCo-LDHs.

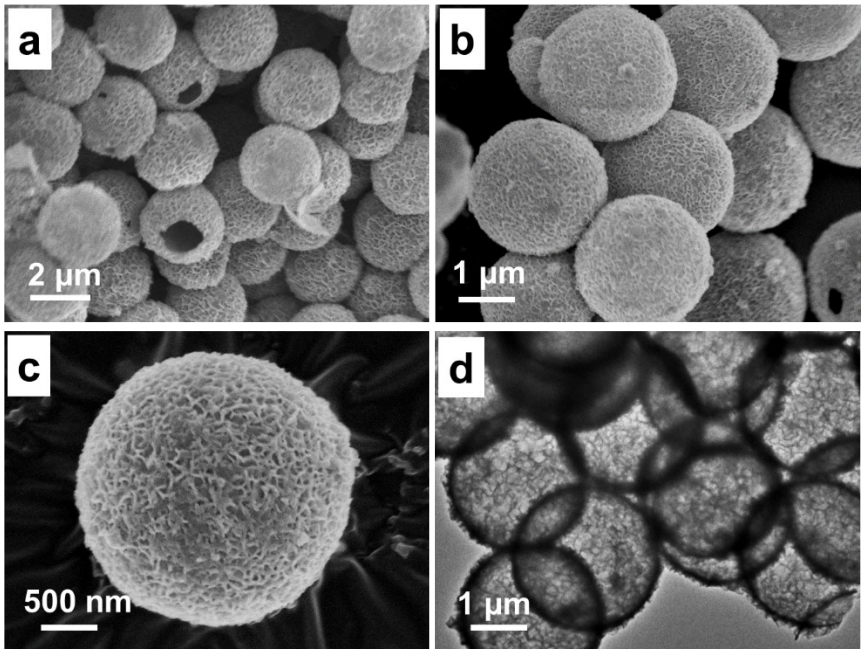

Fig. S4. (a)-(c) SEM images of $Ti_3C_2T_x$@S-NiCoP. (d) TEM image of $Ti_3C_2T_x$@S-NiCoP.

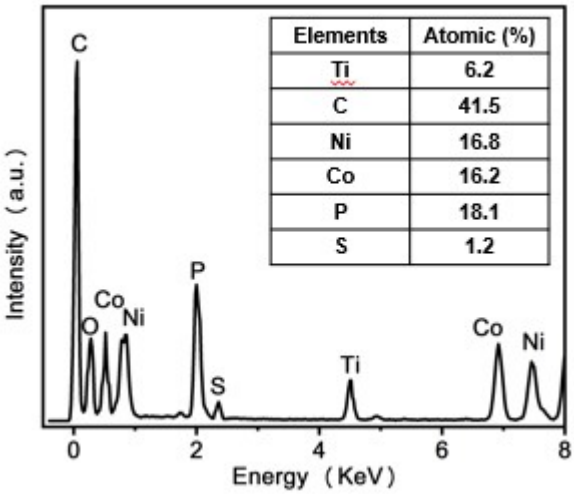

Fig. S5. EDS pattern of the $Ti_3C_2T_x$@S-NiCoP composite with elemental atomic ratio inserted.

Table S1. The elemental content (wt.%) of $Ti_3C_2T_x$@S-NiCoP, $Ti_3C_2T_x$@S-MnP/CoP and $Ti_3C_2T_x$@S-ZnP_2/CoP obtained from ICP-OES results.

Samples	Ti	Co	M	P	S
$Ti_3C_2T_x$@S-NiCoP	8.7	30.3	Ni: 29.1	17.2	1.6
$Ti_3C_2T_x$@S-MnP/CoP	6.2	32.7	Mn:30.9	18.4	1.7
$Ti_3C_2T_x$@S-ZnP_2/CoP	7.7	24.8	Zn:32.2	27.5	2.1

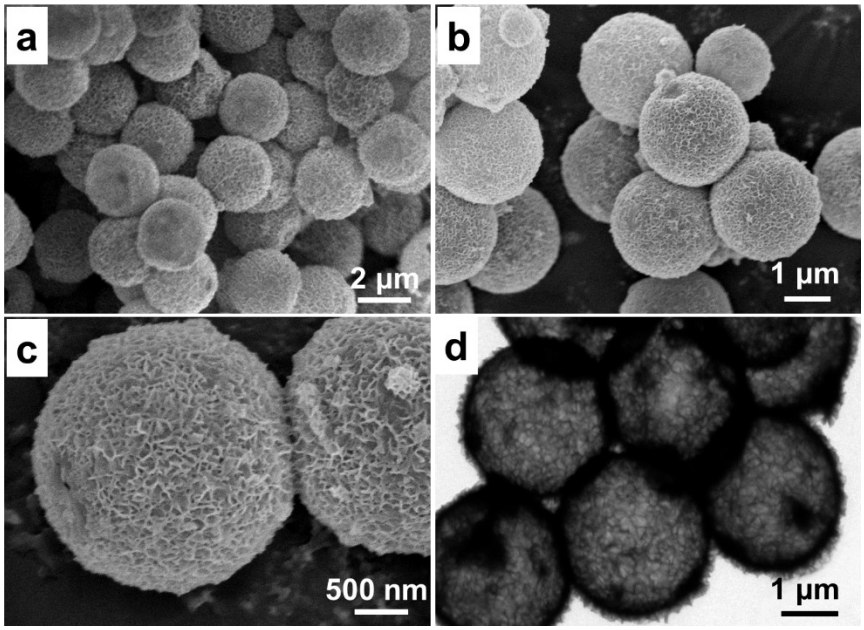

Fig. S6. (a)-(c) SEM images of $Ti_3C_2T_x$@NiCoP. (d) TEM image of $Ti_3C_2T_x$@NiCoP.

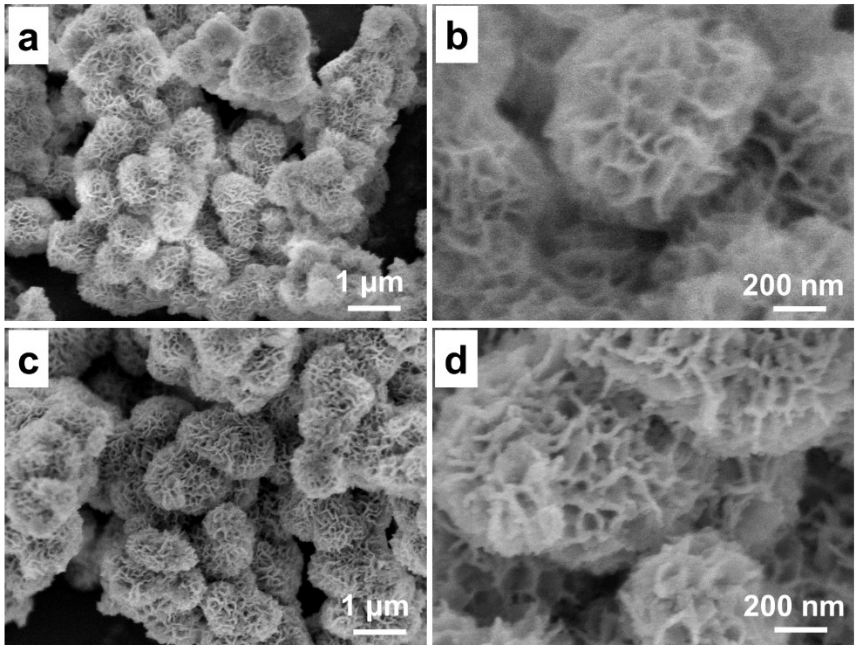

Fig. S7. (a)-(b) SEM images of NiCo-LDHs. (c)-(d) SEM images of S-NiCoP.

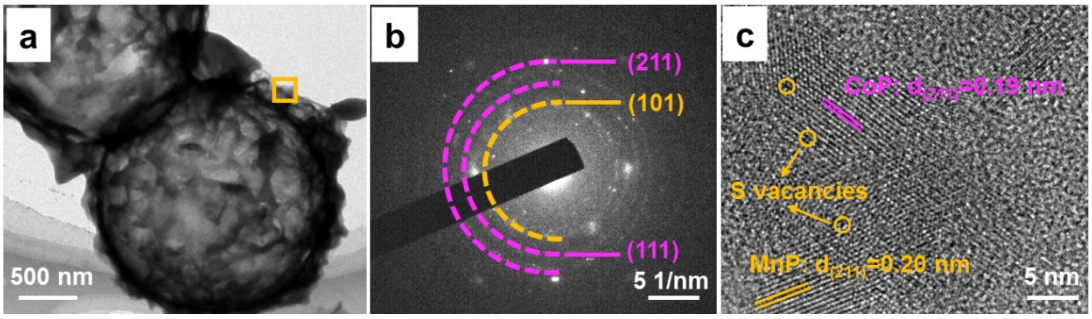

Fig. S8. (a)-(c) TEM, SAED and HRTEM images of $Ti_3C_2T_x$@S-MnP/CoP.

As shown in Fig. S8b, the SAED pattern shows several bright rings, which can be ascribed to the characteristic (101) plane of MnP and the (111) and (211) crystal planes of CoP. Fig. S8c displays the characteristic spacings of 0.19 and 0.20 nm, which can be attributed to the (211) plane of CoP and the (211) plane of MnP, respectively, illustrating the formation of MnP/CoP heterostructure.

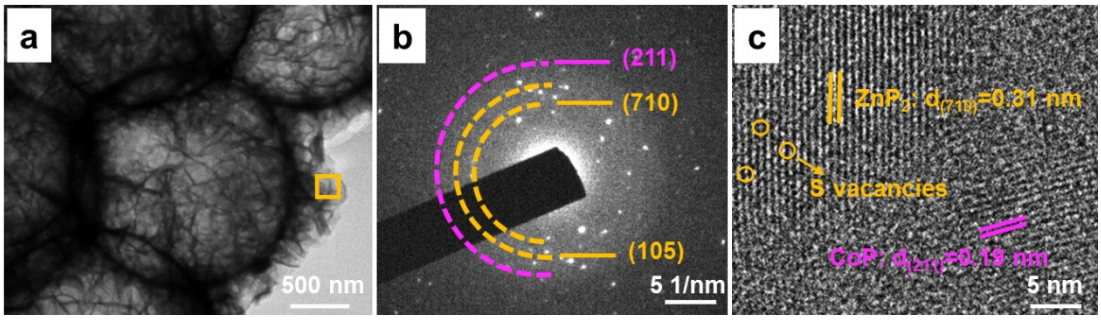

Fig. S9. (a)-(c) TEM, SAED and HRTEM images of $Ti_3C_2T_x$@S-ZnP_2/CoP.

As shown in Fig. S9b, the SAED pattern shows several bright rings, which can be ascribed to the characteristic (710) and (105) planes of ZnP_2 and the (211) crystal plane of CoP. Fig. S9c displays the characteristic spacings of 0.19 and 0.31 nm, which can be attributed to the (211) plane of CoP and the (710) plane of ZnP_2, respectively, also illustrating the formation of ZnP_2/CoP heterostructure.

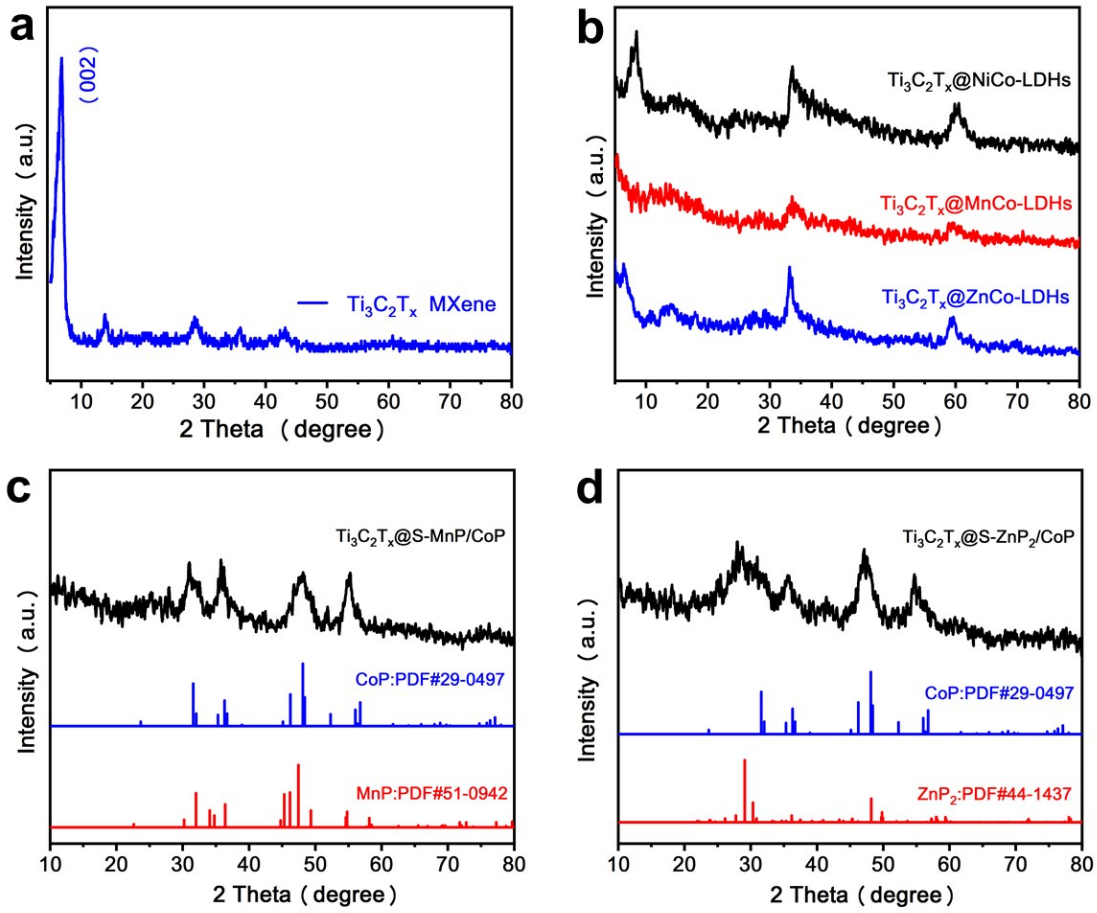

Fig. S10. (a) XRD pattern of $Ti_3C_2T_x$ MXene. (b) XRD patterns of $Ti_3C_2T_x$@NiCo-LDHs, $Ti_3C_2T_x$@MnCo-LDHs and $Ti_3C_2T_x$@ZnCo-LDHs. (c) XRD patterns of $Ti_3C_2T_x$@S-MnP/CoP. (d) XRD patterns of $Ti_3C_2T_x$@S-ZnP_2/CoP.

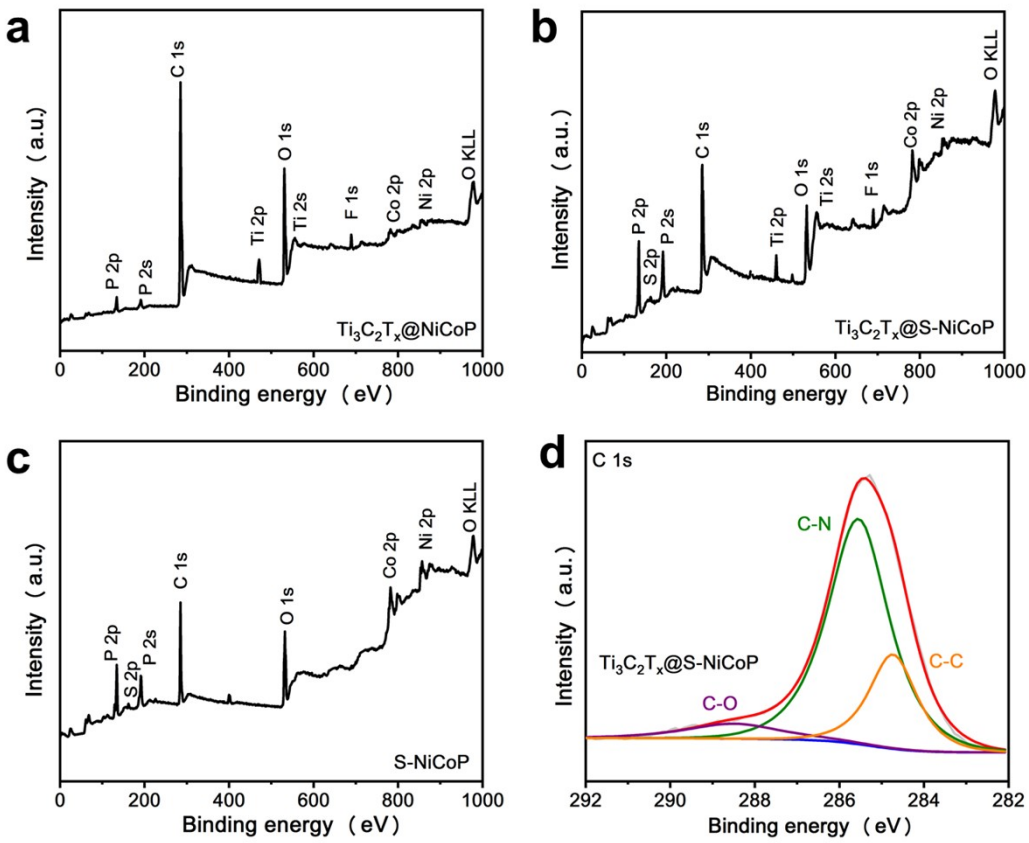

Fig. S11. XPS survey spectra of the as-prepared (a) $Ti_3C_2T_x$@NiCoP, (b) $Ti_3C_2T_x$@S-NiCoP, and (c) S-NiCoP. (d) High-resolution XPS spectra of C 1s for $Ti_3C_2T_x$@S-NiCoP.

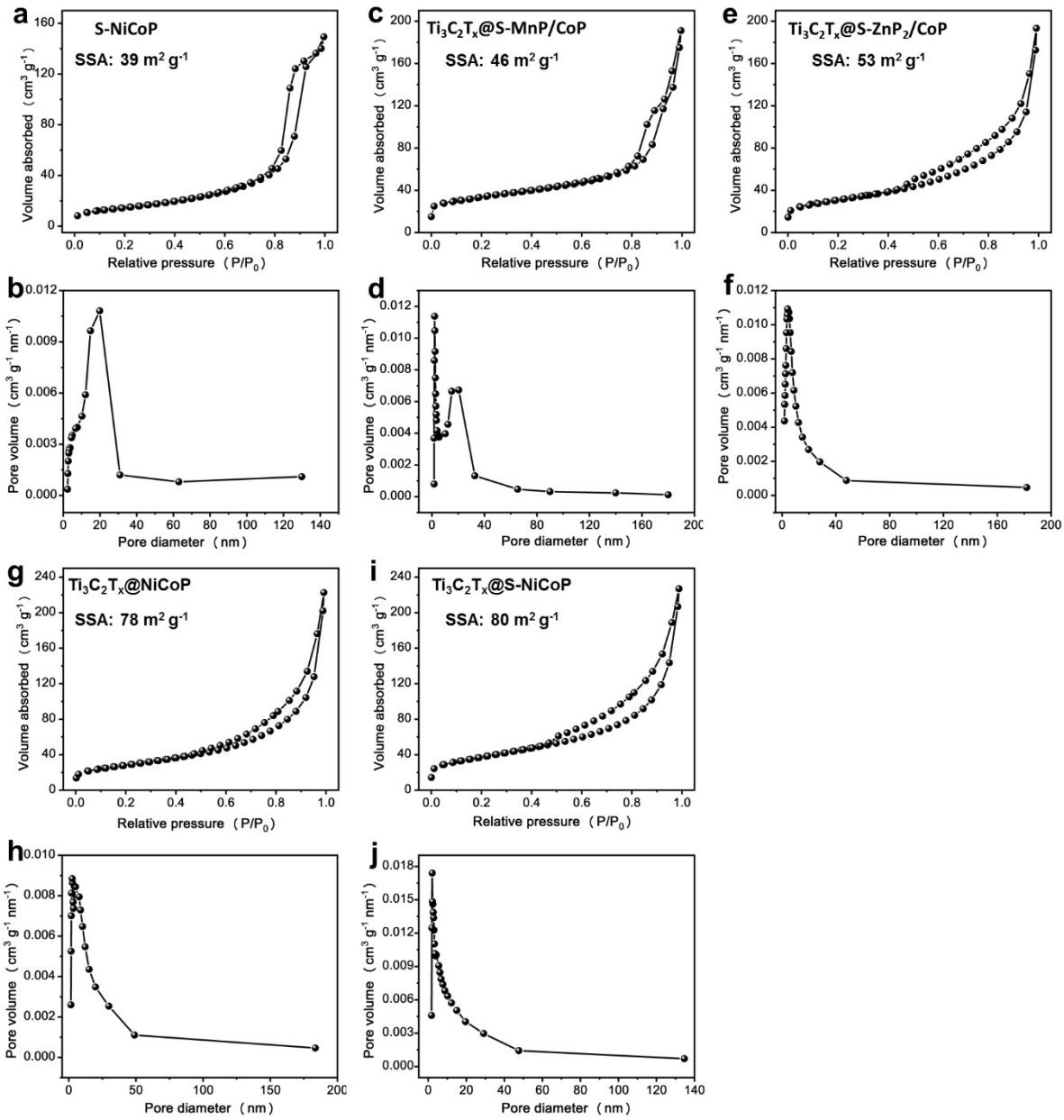

Fig. S12. N_2 adsorption-desorption isotherms and pore size distribution of S-NiCoP (a)-(b), $Ti_3C_2T_x$@S-MnP/CoP (c)-(d), $Ti_3C_2T_x$@S-ZnP_2/CoP (e)-(f), $Ti_3C_2T_x$@NiCoP (g)-(h) and $Ti_3C_2T_x$@S-NiCoP (i)-(j).

As well known, the specific surface areas (SSAs) of active materials are important for their electrochemical performance. As shown in **Fig. S12**, we also used Brunauer-Emmett-Teller test to check SSAs and the pore size distribution of the samples. The calculated SSAs of S-NiCoP, $Ti_3C_2T_x$@S-MnP/CoP, $Ti_3C_2T_x$@S-ZnP_2/CoP,

$Ti_3C_2T_x$@NiCoP and $Ti_3C_2T_x$@S-NiCoP are 39, 46, 53, 78 and 80 m^2/g, respectively.

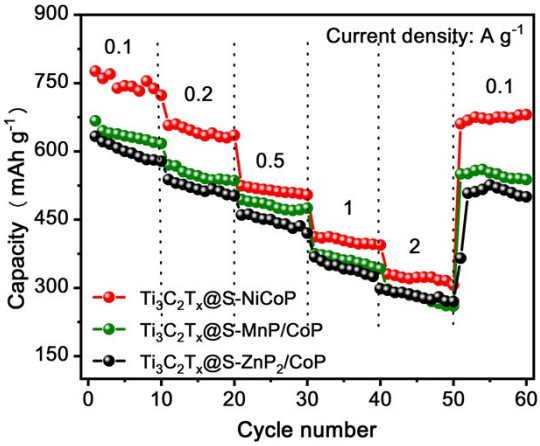

Fig. S13. The rate capability of $Ti_3C_2T_x$@S-NiCoP, $Ti_3C_2T_x$@S-MnP/CoP and $Ti_3C_2T_x$@S-ZnP_2/CoP at different current densities.

As shown in **Fig. S13**, the rate capability of $Ti_3C_2T_x$@S-NiCoP is better than those of $Ti_3C_2T_x$@S-MnP/CoP and $Ti_3C_2T_x$@S-ZnP_2/CoP with specific capacities of 712, 630, 501, 407 and 298 mAh/g at 0.1, 0.2, 0.5, 1 and 2 A/g, respectively.

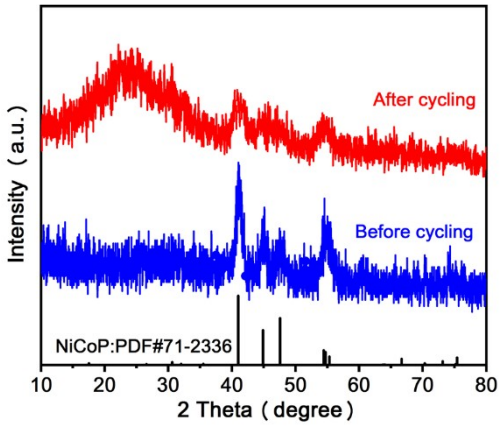

Fig. S14. The XRD patterns of $Ti_3C_2T_x$@S-NiCoP before cycling and after 100 cycles.

As shown in Fig. S14, the XRD patterns of $Ti_3C_2T_x$@S-NiCoP were provided before cycling and after 100 cycles. Compared to before cycling, the XRD signal of $Ti_3C_2T_x$@S-NiCoP becomes weaker after 100 cycles, but still matches the standard card of NiCoP (PDF#71-2336), indicating the excellent structural stability of $Ti_3C_2T_x$@S-NiCoP.

Table S2. Performance comparison of $Ti_3C_2T_x$@S-NiCoP with reported TMPs-based anode materials for SIBs.

Anode materials	Specific Capacity (mAh g^{-1}/A g^{-1})	Rate Capability (mAh g^{-1}/A g^{-1})	Stability (mAh g^{-1}/cycle number/A g^{-1})	Reference
$Ti_3C_2T_x$@S-NiCoP	**563/0.2**	**407/1**	**348/3000/1**	**This work**
GeP/CN[1]	762/0.1	561/1	553/350/0.5	Angew. Chem. Int. Ed., 2021
MnP_4/G20[2]	617/0.5	478/1	446/250/0.5	Adv. Energy Mater., 2021
Sn_4P_3@CNF[3]	712/0.1	496/1	336/500/1	J. Power Source 2020
FeP@NPC[4]	557/0.1	320/1	253/300/1	Energy Storage Mater. 2020
Ti_3C_2/NiCoP[5]	457.9/0.1	278.1/1	267.1/2000/1	Energy Environ. Sci., 2019
Cu_3P@C[6]	286/0.1	215.8/1	156/1000/1	J. Mater. Chem. A, 2019
$Ni_{1.5}Co_{0.5}P_x$[7]	826/0.2	147.9/1	188.9/100/1	Adv. Funct. Mater. 2018

Anode materials	Specific Capacity (mAh g^{-1}/A g^{-1})	Rate Capability (mAh g^{-1}/A g^{-1})	Stability (mAh g^{-1}/cycle number/A g^{-1})	Reference
$Ni_2P/NG/Ni_2P$[8]	331.2/0.5	188.1/1	107.8/400/1	Energy Storage Mater., 2018
FeP@Carbon[9]	400/0.1	237/1.6	/	ACS Nano, 2017,
Ni_2P@C/GA[10]	253.6/0.1	172.1/1	124.5/2000/1	Small, 2017
CoP@C-RGO-NF[11]	473.1/0.1	253.6/0.8	/	Nano Energy, 2017

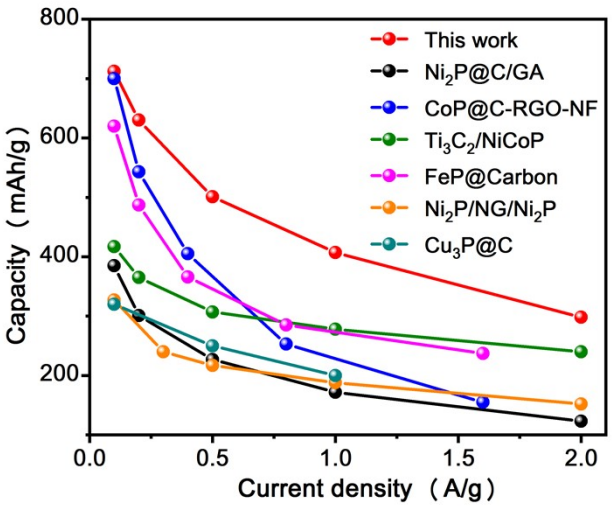

Fig. S15. The rate performance of $Ti_3C_2T_x$@S-NiCoP electrode in comparison with previous reported TMPs.[5-6, 8-11]

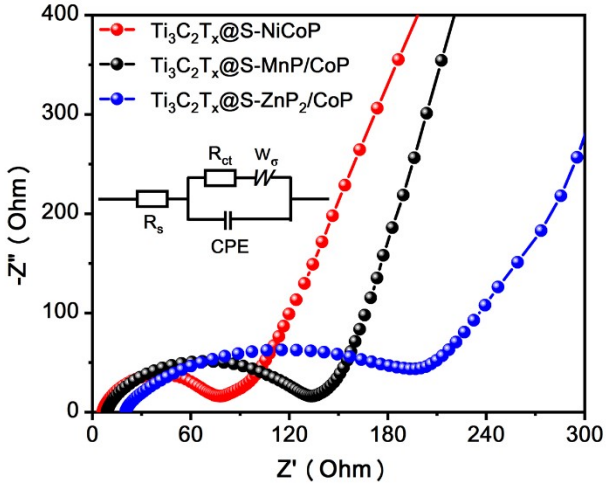

Fig. S16. Nyquist plots of $Ti_3C_2T_x$@S-NiCoP, $Ti_3C_2T_x$@S-MnP/CoP and $Ti_3C_2T_x$@S-ZnP_2/CoP, the inset is the equivalent circuit model.

As shown in **Fig. S15**, the $Ti_3C_2T_x$@S-NiCoP shows smaller Rct value (71 Ω) than those of $Ti_3C_2T_x$@S-MnP/CoP (133 Ω) and $Ti_3C_2T_x$@S-ZnP_2/CoP (208 Ω), verifying the faster charge transfer of $Ti_3C_2T_x$@S-NiCoP, also indicating its better electrochemical performance.

References:

[1] T. Zeng, H. He, H. Guan, R. Yuan, X. Liu and C. Zhang, *Angew. Chem. Int. Ed.*, 2021, **60**, 12103-12108.

[2] K. H. Kim and S. H. Hong, *Adv. Energy Mater.*, 2021, **11**, 2003609.

[3] L. Ran, I. Gentle, T. Y. Lin, B. Luo, N. Mo, M. Rana, M. Li, L. Wang and R. Knibbe, *J. Power Sources*, 2020, **461**, 228116.

[4] S. Shi, Z. Li, L. Shen, X. Yin, Y. Liu, G. Chang, J. Wang, S. Xu, J. Zhang and Y. Zhao, *Energy Storage Mater.*, 2020, **29**, 78-83.

[5] D. Zhao, R. Zhao, S. Dong, X. Miao, Z. Zhang, C. Wang and L. Yin, *Energy Environ. Sci.*, 2019, **12**, 2422-2432.

[6] J. Zhu, Q. He, Y. Liu, J. Key, S. Nie, M. Wu and P. K. Shen, *J. Mater. Chem. A*, 2019, **7**, 16999-17007.

[7] X. Wang, H. Guo, L. Liang, J. Zhang, B. Zhang, J. Wang, W. Luo, H. Liu and S. Dou, *Adv. Funct. Mater.*, 2018, **28**, 1801016.

[8] C. Dong, L. Guo, Y. He, C. Chen, Y. Qian, Y. Chen and L. Xu, *Energy Storage Mater.*, 2018, **15**, 234-241.

[9] X. Wang, K. Chen, G. Wang, X. Liu and H. Wang, *ACS Nano*, 2017, **11**, 11602-11616.

[10] X. Miao, R. Yin, X. Ge, Z. Li and L. Yin, *Small*, 2017, **13**, 1702138.

[11] X. Ge, Z. Li and L. Yin, *Nano Energy*, 2017, **32**, 117-124.